RSC Advances

ROYAL SOCIETY OF CHEMISTRY

www.rsc.org/advances

$Li_4Ti_5O_{12}$ hollow mesoporous microspheres assembled by nanoparticles for high rate lithium-ion battery anodes

Liyun Cao [a], Yani Hui [a], Haibo Ouyang [a], Jianfeng Huang *[a], Zhanwei Xu [a], Jiayin Li [a],

Wanzhuo Zhang [a], Simin Chai [a], Shouwu Guo [a]

a School of Materials Science & Engineering, Shaanxi University of Science and Technology, Xi'an 710021, China

[*]Corresponding author. Tel.: +86 029 86168802; fax: +86 029 86168802.

E-mail: huangjfsust@126.com.

Abstract:

$Li_4Ti_5O_{12}$ hollow mesoporous microspheres (HMMs) assembled by nanoparticles were successfully synthesized by a facile hydrothermal method and following calcinations. They exhibit superior rate capabilities with reversible capacities of 176, 125 and 86 mAh g^{-1} after 10 cycles at 0.1 C, 20 C and 40 C (7000 mA g^{-1}), respectively. The $Li_4Ti_5O_{12}$ HMMs also possess outstanding cycle performances with only 3 % capacity degradation at 10 C after 500 cycles, which is equivalent to a fade of merely 0.006 % per cycle. The comparison with other literatures shows that the $Li_4Ti_5O_{12}$ HMMs possess more promising reversible capacity and rate capability among the values reported for $Li_4Ti_5O_{12}$. These excellent electrochemical properties may be attributed to the unique HMM structures.

Keywords: Lithium titanate; Hollow; Mesoporous; Electrochemical behavior; Lithium-ion batteries.

Introduction

Lithium-ion batteries (LIBs) have become excellent power sources for portable electronic devices and hybrid electric vehicles due to their relatively high energy / power density, low self-discharge and the absence of memory effects [1-5]. The carbon-based material has been commonly adopted as an anode material in most commercial LIBs, since it shows desirable charge potential profile and long cycling life[6, 7]. However, carbonaceous anodes generally suffer from poor coulombic efficiencies at high C-rates and serious safety problems originated from excessive lithium dendrite formation on the anode surface after long-term charge-discharge operations [8-11]. Therefore, there is an urgency to develop alternative anode materials

with improved rate and safety performances. A variety of nanomaterials, such as Co_3O_4 [12, 13], ZnO_2 [14, 15], SnO_2 [16-18], TiO_2 [19, 20], SiO_2 [21, 22] and VO_2 [23, 24] have been intensively investigated as anode materials for LIBs. Nevertheless, most of these materials usually possess poor cycling performance caused by large volume expansion - shrinkage during Li-ion intercalation-extraction reactions, which predisposes the material to pulverization and loss of electrical connectivity [25, 26].

As a promising substitute for graphite, spinel-structured $Li_4Ti_5O_{12}$ has attracted much interest because of several attractive advantages [27-31]. It possesses an extremely flat voltage plateau at about 1.55 V (vs. Li^+/Li), which suppresses the decomposition of electrolyte and the deposition of lithium dendrites, making the LIBs safe [32, 33]. Furthermore, $Li_4Ti_5O_{12}$ also displays excellent cycling stability and outstanding structural stability due to the zero volume change during Li^+ insertion/extraction [25, 34]. However, its low electronic conductivity ($<10^{-13}$ S cm^{-1}) and Li^+ diffusion coefficient (10^{-9} - 10^{-13} cm^2 s^{-1}) result in poor rate performance [35, 36], which limits its practical applications in the fields of electric vehicles and hybrid electric vehicles.

In recent years, extensive efforts have been devoted to improve the rate capability of $Li_4Ti_5O_{12}$, and one of the most common strategies is to fabricate nanostructured $Li_4Ti_5O_{12}$ [37-39]. Since the diffusion capability of the ion is in inverse proportion to square of particle size and in proportion to diffusion coefficient [40], the decrease in the grain size can significantly enhance the rate performance of $Li_4Ti_5O_{12}$. Up to now, the mesoporous structure assembled by nanounits has been regarded as an ideal host for the rapid transportation of both ions and electrons in high-rate LIBs [41-43],

as it possesses both the advantages of nanometer-sized building blocks (e.g., shortened diffusion distance and high specific area) and micrometer-sized assemblies (e.g., excellent thermodynamic stability and high tap-density), benefiting for cycling and rate performances [44]. Moreover, its porosity structures would allow electrolyte to penetrate easily, which makes the Li^+ insertion/extraction more sufficiently [45].

In order to further optimize the structures and electrochemical performances of mesoporous microsphere, such as decrease its density and make the best of its central nanounits, more and more researchers turned their attention to the preparation of hollow mesoporous microspheres. $Li_4Ti_5O_{12}$ hollow microspheres assembled by nanoparticles [46] or nanosheets [47] have been successfully prepared, exhibiting superior high rate capability and great cycling stability. However, templates or high reaction temperatures are usually needed in the system, which makes the synthetic process complicated and costly. Therefore, in this work, we employed a facile hydrothermal method and following calcinations yielding unique $Li_4Ti_5O_{12}$ hollow mesoporous microspheres (HMMs) assembled by nanoparticles without templates or surfactants. The obtained $Li_4Ti_5O_{12}$ HMMs, used as anode materials in LIBs, exhibited superior cycle and rate performances.

Experimental

Material preparation

$Li_4Ti_5O_{12}$ HMMs were synthesized by a hydrothermal process and following calcinations. The lithium hydroxide monohydrate ($LiOH·H_2O$) was purchased from China National Medicines Corp., Ltd. The precursor TiO_2 was prepared using the

4

method in Ref. [48]. Typical, 0.5 g TiO_2 was added into a 40 ml 2 M LiOH solution under magnetic stirring for 30min. The mixture was transferred into a 100 ml Teflon-lined autoclave in a homogeneous reactor at 160 °C for 48 hours. After cooling down naturally, the resulting precipitate was collected by centrifugation and washed thoroughly with deionized water for several times. Eventually, the obtained products after hydrothermal process was calcined at 400 °C (200 °C, 600 °C and 900 °C are shown in Supporting Information) for 2 h.

Materials characterization

Crystal structures of the prepared samples were characterized by X-ray diffraction (XRD) using an X-ray powder diffractometer (Rigaku D/max-2200PC). X-ray profiles were recorded between 15 and 70° (2θ) with with Cu Kα radiation (λ =1.5406 Å). The Raman spectra were recorded with a confocal microprobe Raman system (Renishaw-invia with a laser at 532 nm). Particle sizes, morphologies, and microstructures of the samples were observed by using a field - emission scanning electron microscope (FESEM, S-4800) and a transmission electron microscope (TEM, TecnaiG^{2}F20S-TWIN). Nitrogen adsorption/desorption isotherms were acquired at 77K using a surface area and pore size analyser (NOVA 2200e). Specific surface areas were calculated based on the Brunauer-Emmett-Teller (BET) method. The Barrett-Joyner-Halenda (BJH) pore size distribution was determined from the desorption isotherms. Thermal gravimetric-differential scanning calorimetry analysis (TGA-DSC) was performed on a STA409PC, in nitrogen with a heating rate of 10 °C min^{-1}.

Electrochemical measurements

Electrochemical measurements were performed using CR2032 coin-type cells assembled in an argon-filled glove box. To prepare anode materials as working electrode, the synthesized $Li_4Ti_5O_{12}$, polyvinylidene fluoride (PVDF) binder and acetylene black were mixed together at a weight ratio of 80:10:10 in N-methylpyrrolidinone (NMP). The slurry was then coated onto copper foil. After vacuum drying at 80 $^{\circ}$C for 24 h, electrode discs with a diameter of 16 mm (area of about 2 cm^2) were punched out and weighed. The mass of $Li_4Ti_5O_{12}$ material was around 3.0 mg. The electrolyte consisted of a solution of 1 M $LiPF_6$ in ethylene carbonate and dimethyl carbonate (EC+DMC, 1:1 in volume). The electrochemical performance of the $Li_4Ti_5O_{12}$ HMM was examined with lithium as counter electrode. The capacity and cycle performance were evaluated by a multichannel battery testing system (Shenzhen, Neware, China) with a potential window ranging from 1.0 to 2.5 V at various current densities. Cyclic voltammograms (CV) were recorded at scan rates of 0.05 mV / s, using CHI660E electrochemical station (Shanghai Chenhua, China). All above electrochemical measurements were taken at room temperature.

Results and discussion

Structure and morphology
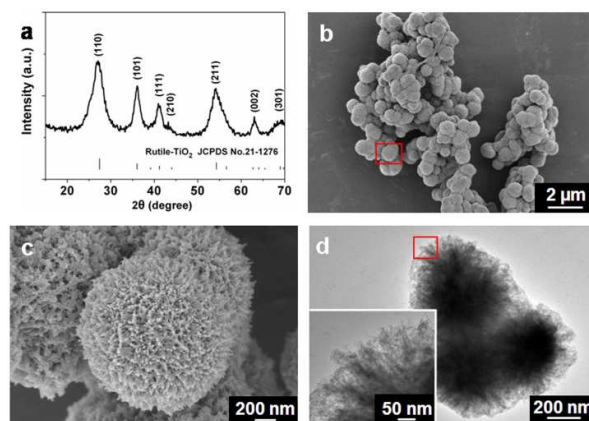
Fig. 1 XRD patterns (a), SEM images (b) and (c), TEM images (d) of the precursor TiO$_2$. (inset: magnified TEM image of the second red rectangle)

X-ray diffraction (XRD) analysis was employed to investigate the precursor phases. The XRD patterns of the precursor TiO$_2$ is shown in Fig. 1a. It is found that the titanium source in this experiment is pure rutile TiO$_2$ and the wide diffraction peaks may imply the grain size is very small. The morphology and microstructure of the precursor was examined by SEM and TEM. Fig. 1b shows a SEM image of the TiO$_2$, which is composed of microspheres with a rough surface. Many of the microspheres are closely connected, and the diameter of the microsphere is around 1.3 μm. Fig. 1c and 1d reveal that the TiO$_2$ microsphere is actually is comprised of the assembly of interconnected nanorods with a diameter of about 20 nm. The nanocrystallite sizes are in good agreement with that estimated from XRD.

The XRD patterns of the products after hydrothermal process (PAHP) and the Li$_4$Ti$_5$O$_{12}$ calcined at temperatures of 300 $^\circ$C, 600 $^\circ$C and 900 $^\circ$C are shown in Fig. S1 (Electronic Supplementary Information, ESI), while the Li$_4$Ti$_5$O$_{12}$ calcined at 400 $^\circ$C is shown in Fig. 2a. It is found that the calcination temperature greatly affected the crystal phases of the final products. As shown in Fig. S1, the diffraction peaks of the

PAHP conform to a $LiTiO_2$ (JCPDS No.16-0223) without obvious impurity phase. After calcination at 300 $^{\circ}$C, the final products exhibit a weak and broadened peak at approximately 18.3 $^{\circ}$, which can be indexed to spinel $Li_{1+x}Ti_{2-y}O_{4+\delta}$ [49]. When the calcination temperature rises to 400 $^{\circ}$C, all the diffraction peaks of the final products correspond well with a face-centered cubic spinel structure of $Li_4Ti_5O_{12}$ (JCPDS No.49-0207), which indicates that the PAHP is completely converted into the crystallized spinel $Li_4Ti_5O_{12}$. Eventually, the $Li_4Ti_5O_{12}$ is partly decomposed into $LiTiO_2$ and TiO_2 after calcined at 900 $^{\circ}$C.
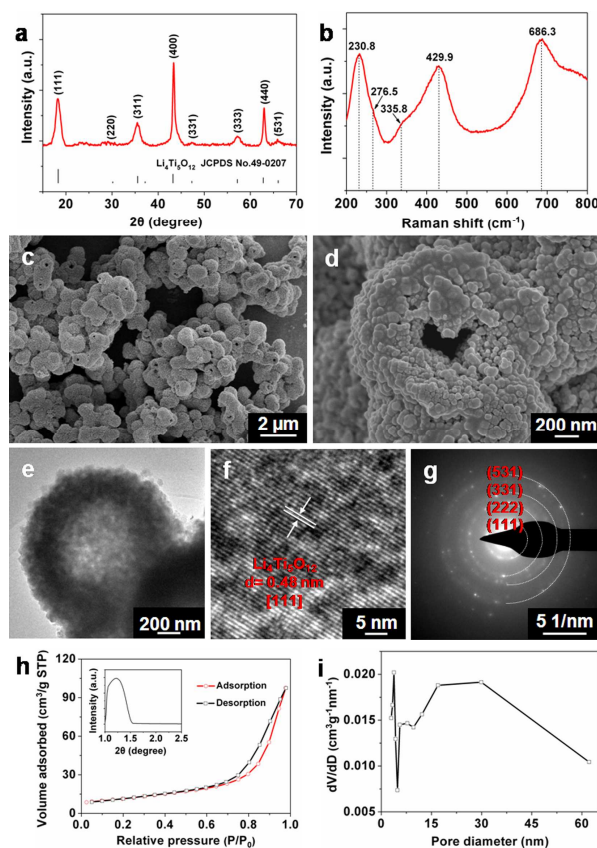
Fig. 2 XRD patterns (a), Raman spectrum (b), SEM images (c) and (d), TEM images (e), HRTEM images (f), SAED patterns (g), Nitrogen adsorption / desorption isotherms, small-angle XRD patterns (inset) (h) and pore size distribution (i) of the

$Li_4Ti_5O_{12}$.

Moreover, the TG-DSC test of the products after hydrothermal process is shown in Fig. S2 (ESI). The TG curve in Fig. S2 shows a weight loss of around 13% from room temperature to 300 °C. As can be seen in the DSC curve, there is an obvious endothermal peak at 200 - 400 °C and an exothermal peak at approximately 900 °C in the DSC curves. Correspond to the TG curve, the flat plateau around 400 °C indicates the formation of $Li_4Ti_5O_{12}$ which is confirmed in the XRD pattern of the 400 °C product. The beginning of the $Li_4Ti_5O_{12}$ decomposition locates at the range of 600~800℃.

The structure of $Li_4Ti_5O_{12}$ calcined at 400 °C is further confirmed by the results of Raman spectrum plotted in Fig. 2b. The products exhibit five vibration peaks at 230.8, 276.5, 335.8, 429.9 and 686.3 cm⁻¹, which can be indexed to the $A_{1g}+E_g+3F_{2g}$ spinel structure. The peak at 686.3 cm⁻¹ is characteristic of A_{1g} mode, which can be assigned to Ti-O stretches in "TiO_6" octahedral. The peak at 429.9 cm⁻¹ is ascribed to E_g mode, and the other three peaks are F_{2g} modes [28]. In addition, no obvious peaks were detected, confirming the high purity phase in the products. It was demonstrated that spinel $Li_4Ti_5O_{12}$ without any distinct impurities could be obtained after the calcinations at 400 °C greatly lower than the solid state synthesis c[7, 8, 33, 34, 45-47, 49, 50].

To further examine the architecture of the $Li_4Ti_5O_{12}$, the samples were investigated by SEM, TEM and HRTEM. The SEM images of the PAHP and the $Li_4Ti_5O_{12}$ calcined at temperatures of 300 °C, 600 °C and 900 °C are shown in Fig. S3 (ESI), while the $Li_4Ti_5O_{12}$ calcined at 400 °C is shown in Fig. 2c and d. It shows that

the morphologies of PAHP turn out to be hollow microspheres, the shells of which are assembled by many nanoparticles. Similar hollow microsphere structure can be obtained after calcined at 300 $^\circ$C, 400 $^\circ$C and 600 $^\circ$C, except for 900 $^\circ$C, as shown in Fig. 2c and Fig. S3. Fig. 2c shows that the $Li_4Ti_5O_{12}$ HMMs are about 1.2 μm in diameter, with a shell thickness of approximately 400nm. Upon closer examination the shell was found to be assembled by thousands of nanoparticles with the size of around 60 nm (Fig. 2d). Furthermore, many of the microspheres are broken and the cavities can be clearly seen from Fig. 2c. Further evidence for the hollow structure can also be found from Fig. 2e. The TEM image of the $Li_4Ti_5O_{12}$ HMMs is shown in Fig. 2e. The clear contrast between the dark edge and the gray center of each microsphere reveals its hollow nature; the gray parts and white spots in the center of every microsphere confirms the presence of porous structure. The HRTEM image in Fig. 2f shows that the interplanar distance between adjacent lattice fringes is 0.48 nm, corresponding to the (111) interplanar spacing of spinel $Li_4Ti_5O_{12}$, which indicates the $Li_4Ti_5O_{12}$ HMMs are assembled by the well-crystallized spinel $Li_4Ti_5O_{12}$ nanoparticles [50]. The clear contrast of light and shade between the primary particles can be found in the HRTEM image shown in Fig. S4 (ESI), indicating the presence of three-dimensionally interconnected mesopores in the $Li_4Ti_5O_{12}$ HMMs. The formation mechanism of the hollow structured $Li_4Ti_5O_{12}$ was presented in ESI. The corresponding selected area electron diffraction (SAED) pattern is demonstrated in Fig. 2g, which can be indexed to the diffraction planes of (111), (222), (331) and (531) of the spinel $Li_4Ti_5O_{12}$ phase, suggesting the polycrystalline nature of the $Li_4Ti_5O_{12}$

HMMs.

N$_2$ adsorption/desorption analysis was used to examine the mesoporous structure of Li$_4$Ti$_5$O$_{12}$, as shown in Fig. 2h. The isotherm curve seemed to be the intermediate between type II and IV [51] with an H$_3$ hysteresis loop, which exhibited the hysteresis loop beginning at relative pressures of P/P$_0$= 0.44, but without dramatic flat desorption isotherms at high relative pressures of P/P$_0$= 0.9-1.0. The small-angle XRD patterns of Li$_4$Ti$_5$O$_{12}$ is illustrated in the inset of Fig. 2h. It is seen that the Li$_4$Ti$_5$O$_{12}$ presented one intense diffraction peak, indicating that a well-organized mesoporous structure was formed [44], which was also confirmed by TEM micrographs (Fig. 2e) and HRTEM micrographs (Fig. S4). The Barrett-Joyner-Halenda (BJH) pore size distribution of the Li$_4$Ti$_5$O$_{12}$, shown in Fig. 2i, indicated that the mesoporous Li$_4$Ti$_5$O$_{12}$ materials exhibited a broad range of pore sizes (2.9 - 62.1 nm) distribution, with the average pore diameter of 3.8 nm. According to Brunauer-Emmett-Teller (BET) analysis, a large specific surface area of 86.5 m^{2}g^{-1} is obtained, benefiting its lithium storage [52, 53].

Electrochemical performance

To test the potential application of the Li$_4$Ti$_5$O$_{12}$ HMMs in Li ion batteries, we investigated their electrochemical performance toward Li insertion/extraction. Fig. 3a shows the first three consecutive cyclic voltammograms of the Li$_4$Ti$_5$O$_{12}$ HMM electrodes at a scan rate of 0.05 mV s^{-1} in the potential range from 2.5 to 1.0 V (vs Li$^+$ / Li). The reduction/oxidation peaks around 1.55 V can be observed during the charge/discharge process, which indicates the characteristic of the two-phase reaction

between $Li_7Ti_5O_{12}$ and $Li_4Ti_5O_{12}$ [52]. Meanwhile, the three CV curves are over-lapped,

suggesting excellent cycle stability.
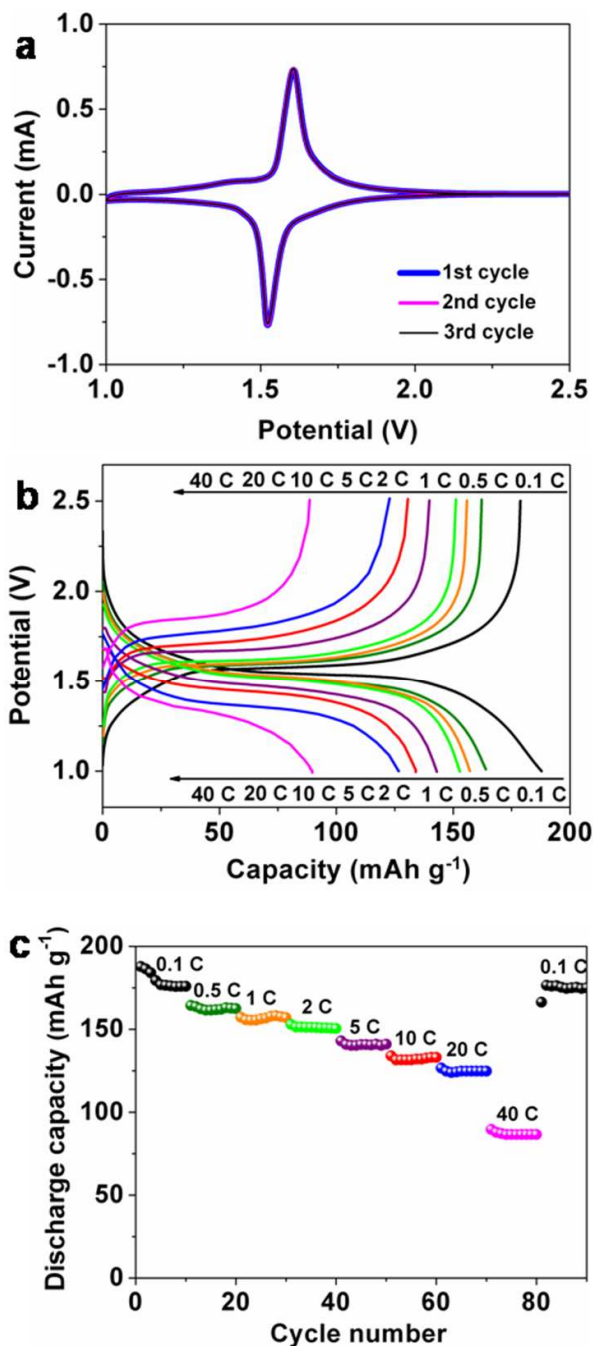
Fig. 3 The first three consecutive cyclic voltammograms of the $Li_4Ti_5O_{12}$ (a); initial

charge/discharge curves of the $Li_4Ti_5O_{12}$ at 0.1-40 C (b); rate properties of the

$Li_4Ti_5O_{12}$ at 0.1-40 C (c).

Fig. 3b presents the charge / discharge profiles of the $Li_4Ti_5O_{12}$ HMM electrodes

cycled at current rates from 0.1 to 40 C. The charge / discharge voltage profiles show

a pair of voltage plateaus at the potential around 1.55 V, which is consistent with the

CV results. The initial discharge and charge capacities at 0.1 C are 188 and 179 mAh

g^{-1}, corresponding to the initial coulombic efficiency (charging capacity / discharging

capacity) of 95 %, implying little initial irreversible capacity loss. The high initial

coulombic efficiency and charging / discharging capacity indicate that lithium ions

could almost totally extract after lithium insertion and the active sites would be nearly

fully utilized. With increasing of the charge / discharge rates, the potential differences

between charge and discharge plateaus exhibit a tendency to increase which could be

attributed to the increased electrode polarization and the sluggish diffusion kinetics of

Li-ion at high rates [6].

The corresponding rate performance is shown in Fig. 3c. It was tested at 0.1C for

the first 10 cycles, and then, the rate was increased to 40 C. At the rate of 0.1C, the

discharge capacity is gradually decrease from 188 to 176 mAh g^{-1} within the first 4

cycles. However the discharge capacities remain stable maintaining a value of 176

mAh g^{-1} for the next 6 cycles. The discharge capacity of the $Li_4Ti_5O_{12}$ HMM

electrodes at 0.1 C is slightly higher than its theoretical value (175.4 mAh g^{-1}); many

researchers have reported this phenomenon as well [28, 33, 38]. It may be due to the

electrode material's unique morphology, large surface area, lattice defect, or impurity

phases within the electrode materials. The discharge capacity of 163 mAh g^{-1} is

obtained at a rate of 0.5 C after 10 cycles; the capacities are 157, 151, 141, 133, 125

13

and 86 mAh g^{-1} when tested at 1, 2, 5, 10, 20 and 40 C, respectively. It is worth noting

that the capacity can be completely recovered to 174 mAh g^{-1} when the discharge rate

returns to 0.1 C rate after continuous 40 C rate cycles, indicating its good

electrochemical reversibility even after high rate discharge-charge cycles. The

comparison of rate properties between the three samples annealed at 300 (LTO - 300),

400 (LTO - 400, Li$_4$Ti$_5$O$_{12}$ HMM electrodes) and 600 °C (LTO - 600) is shown in Fig.

S6 (ESI). It shows that the LTO - 400 exhibited significantly better rate performance

than LTO - 300 and LTO - 600; the discharge capacities were in the following

descending order: LTO - 400 > LTO - 600 > LTO - 300.
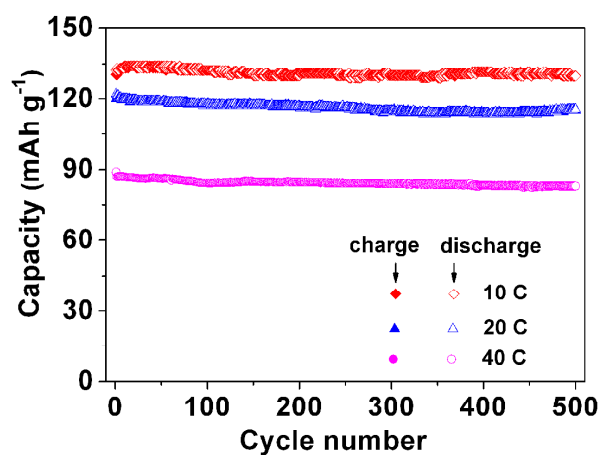
Fig. 4 Cycling performance for the 500 cycles at the rates of 10 C, 20 C and 40 C,

respectively.

Cycling performance of the Li$_4$Ti$_5$O$_{12}$ HMM electrodes at 10 C, 20 C and 40 C is

illustrated in Fig. 4. The corresponding coulombic efficiency is shown in Fig. S4. At

the rate of 10C, the discharge capacity gradually increases from 132 to 134 mAh g^{-1}

between the 1st and 10th cycles and decreases from 134 to 130 mAh g^{-1} after the next

490 continuous cycles with only 3 % degradation, which is equivalent to a capacity

fade of merely 0.006 % per cycle. They also exhibit reversible capacities 115 and 83 mAh g^{-1} after 500 cycles at 20 C and 40 C, respectively. As can be seen that capacity of the $Li_4Ti_5O_{12}$ HMM electrodes remain stable, when the C rate increases, which may be due to that only part of the electrode material with the most electrochemical active actually charge / discharge in the test since Li^+ ions and electrons don't have abundant time to diffuse and to conduct in the particles at higher C rate [2]. The coulombic efficiencies at 10 C, 20 C and 40 C all stabilize above 99% between the 1st and 500th cycles, as shown in Fig. S5 (ESI). These results demonstrate excellent cycling performance of the $Li_4Ti_5O_{12}$ HMM electrodes even at the rate of 40 C.
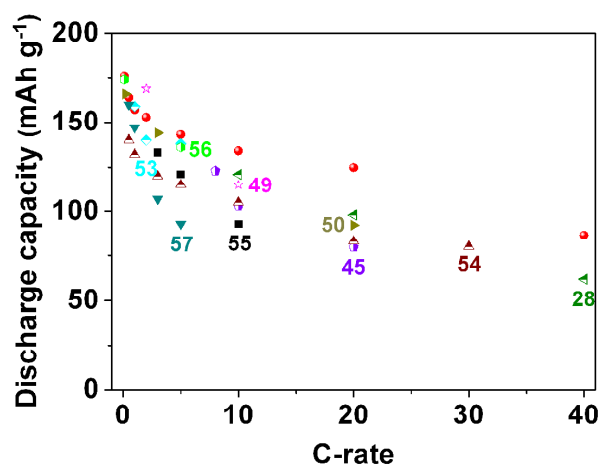
Fig. 5 Discharging capacity performance comparison of $Li_4Ti_5O_{12}$ HMM electrodes with recently reported $Li_4Ti_5O_{12}$ electrodes, all tested as half cells vs. Li / Li^+.

Table 1 Discharging capacity performance comparison of $Li_4Ti_5O_{12}$ HMM electrodes with recently reported $Li_4Ti_5O_{12}$ electrodes, all tested as half cells vs. Li/Li^+.

Material Content	Synthesis Method	Microstructure	Capacity* (mAh g^{-1})	C rate	Current Collector	References

Pure $Li_4Ti_5O_{12}$	Hydrothermal method and following calcinations	HMMs assembled by nanoparticles	157 (10)	1 C	Copper foil	This work
			133 (10)	10 C		
			125 (10)	20 C		
			86 (10)	40 C		
Pure $Li_4Ti_5O_{12}$	Microwave-assisted hydrothermal and microwave post annealing process	Microspheres composed of nanoflakes	121 (10)	10 C	Copper foil	Chou et al [28]
			98 (10)	20 C		
			62 (10)	40 C		
$Li_4Ti_5O_{12}$ with tiny amounts of TiO_2	Molten salt process	Hierarchical mesoporous microspheres	123 (10)	8 C	Copper foil	Nugroho et al [45]
			103 (10)	10 C		
			80 (10)	20 C		
$Li_4Ti_5O_{12}$ with little amounts of TiO_2	Solvothermal method and following calcinations	Mesoporous microspheres	169 (initial)	2 C	Aluminium plate	Lin et al [49]
			115 (initial)	10 C		
$Li_4Ti_5O_{12}$ with small amounts of Li_2TiO_3	Hydrothermal synthesis and following calcinations	Hierarchically porous microspheres	166 (10)	0.2 C	Aluminium foil	Shen et al [50]
			144 (10)	3 C		
			92 (10)	20 C		
Pure $Li_4Ti_5O_{12}$	Hydrothermal synthesis and following calcinations	Mesoporous	120 (20)	3 C	Never mentioned	Lin et al [54]
			105 (20)	10 C		
			83 (20)	20 C		
			80 (20)	30 C		
$Li_4Ti_5O_{12}$ with little amounts of Li_2CO_3	coprecipitation method and following calcinations	Mesoporous nanoclusters	159 (5)	1 C	Copper foil	Sun et al [53]
			140 (5)	2 C		
			138 (5)	5 C		
Pure $Li_4Ti_5O_{12}$	High-energy ball milling process	Microsized particle	133 (5)	3 C	Aluminium foil	Liu et al [55]
			121 (5)	5 C		
			93 (5)	10 C		
Pure	Spray drying	nanosized	174 (initial)	0.1 C	Copper foil	He et al [56]

16

Li$_4$Ti$_5$O$_{12}$	process	particle	136 (initial)	5 C		
			160 (20)	0.5 C		
Pure Li$_4$Ti$_5$O$_{12}$	Sol-gel strategy	Monodispersed mesoporous	107 (20)	3 C	Never mentioned	Lin et al [57]
			93 (20)	5 C		

*The capacity after (X) cycles.

Fig. 5 and Table 1 compare the discharging capacity performance of Li$_4$Ti$_5$O$_{12}$ HMM electrodes with recently reported Li$_4$Ti$_5$O$_{12}$ electrodes [28, 45, 49, 50, 53-57]. In order to make the table not too large, Table 1 only shows a part of the discharging capacity values. Fig. 5 graphically contrasts the discharging capacity versus C rates, indicating promising rate characteristics of the Li$_4$Ti$_5$O$_{12}$ HMM electrodes.

It is well known that the morphology and particle size have important effects on the electrochemical properties of Li$_4$Ti$_5$O$_{12}$. The HMM structure of Li$_4$Ti$_5$O$_{12}$ have several merits to account for the excellent lithium storage properties and the much improved rate performances. Firstly, the open HMM structure (about 400 nm in diameter) would allow lithium (around 0.1 nm in diameter [58]) to insert into the Li$_4$Ti$_5$O$_{12}$ particles from both inside and outside, which makes it more effective for lithium intercalation. Secondly, the large amount of pores, with average pore diameter of 3.8 nm, is desirable to accommodate a great number of Li ions within the pore not only by surface adsorption. This thesis has been proved in Ref. [59]. Thirdly, the interconnected nanoparticles could increase electrode / electrolyte contact areas and short diffusion paths for both Li$^+$ and electrons within particles. The interconnected nanoparticles also significantly decrease their contact resistance, this view has been confirmed in Ref. [60], thereby enhancing the high rate performance of Li$_4$Ti$_5$O$_{12}$ HMM

electrodes.

Conclusions

In summary, we obtained $Li_4Ti_5O_{12}$ HMMs by a hydrothermal method and following calcinations. The $Li_4Ti_5O_{12}$ HMMs are about 1.2 μm in diameter, and their shells are assembled by thousands of nanoparticles with the size of around 60 nm. Moreover, they deliver a reversible capacity as high as 176 mAh g^{-1} at the C rate of 0.1 C after 10 cycles. The $Li_4Ti_5O_{12}$ HMM electrodes also exhibit reversible capacities 130, 115 and 83 mAh g^{-1} after 500 cycles at 10 C, 20 C and 40 C, respectively. A comparison with recently reported $Li_4Ti_5O_{12}$ electrodes reveals that these performance matrices are highly favorable, indicating their promising applications for high power LIBs in the future.

Acknowledgements

Reference

1.   M. Armand and J.-M. Tarascon, *Nature*, 2008, **451**, 652.
2.   C. Lin, X. Fan, Y. Xin, F. Cheng, M. O. Lai, H. Zhou and L. Lu, *J. Mater. Chem. A*, 2014, **2**, 9982.
3.   M. Chen, W. Li, X. Shen and G. Diao, *ACS Appl. Mater. Interfaces*, 2014, **6**, 4514.
4.   J. Haruyama, K. Sodeyama, L. Han, K. Takada and Y. Tateyama, *Chem. Mater.*, 2014, **26**, 4248.
5.   Q. Yue, H. Jiang, Y. Hu, G. Jia and C. Li, Chem. Commun.,2014, **50**, 13362.
6.   T. F. Yi, Z. K. Fang, Y. Xie, Y. R. Zhu and S. Y. Yang, *ACS Appl. Mater. Interfaces*, 2014, **6**,

20205.

7.   X. Li, H. C. Lin, W. J. Cui, Q. Xiao and J. B. Zhao, *ACS Appl. Mater. Interfaces*, 2014, **6**, 7895.

8.   S. Chen, Y. Xin, Y. Zhou, Y. Ma, H. Zhou and L. Qi, *Energy Environ. Sci.*, 2014, **7**, 1924.

9.   J. Hassoun, F. Bonaccorso, M. Agostini, M. Angelucci, M. G. Betti, R. Cingolani, M. Gemmi, C. Mariani, S. Panero, V. Pellegrini and B. Scrosati, *Nano Lett.*, 2014, **14**, 4901.

10.   Z. Jian, M. Zheng, Y. Liang, X. Zhang, S. Gheytani, Y. Lan, Y. Shi and Y. Yao. *Chem. Commun.*,2015, **51**, 229.

11.   J. W. Lee, S. Y. Lim, H. M. Jeong, T. H. Hwang, J. K. Kang and J. W. Choi, *Energy Environ. Sci.*, 2012, **5**, 9889.

12.   W. H. Ryu, T. H. Yoon, S. H. Song, S. Jeon, Y. J. Park and I. D. Kim, *Nano Lett.*, 2013, **13**, 4190.

13.   J. Jiang, Y. Li, J. Liu, X. Huang, C. Yuan and X. W. Lou, *Adv. Mater.*, 2012, **24**, 5166.

14.   D. Bresser, F. Mueller, M. Fiedler, S. Krueger, R. Kloepsch, D. Baither, M. Winter, E. Paillard and S. Passerini, *Chem. Mater.*, 2013, **25**, 4977.

15.   Y. Feng, R. Zou, D. Xia, L. Liu and X. Wang, *J. Mater. Chem. A*, 2013, **1**, 9654.

16.   J. H. Kang, S. M. Paek and J. H. Choy, *Chem. Commun.*, 2012, **48**, 458.

17.   L. Wang, D. Wang, Z. Dong, F. Zhang and J. Jin, *Nano Lett.*, 2013, **13**, 1711.

18.   P. Wu, N. Du, H. Zhang, C. Zhai and D. Yang, *ACS Appl. Mater. Interfaces*, 2011, **3**, 1946.

19.   J. Qiu, P. Zhang, M. Ling, S. Li, P. Liu, H. Zhao and S. Zhang, *ACS Appl. Mater. Interfaces*, 2012, **4**, 3636.

20.   Y. Fu and J. Shen, *Chem. Commun.*, 2007, 2172.

21.   H. Wu, G. Zheng, N. Liu, T. J. Carney, Y. Yang and Y. Cui, *Nano Lett.*, 2012, **12**, 904.

22.   B. Liu, A. Abouimrane, Y. Ren, M. Balasubramanian, D. Wang, Z. Z. Fang and K. Amine, *Chem. Mater.*, 2012, **24**, 4653.

23.   S. J. Chang, J. B. Park, G. Lee, H. J. Kim, J. B. Lee, T. S. Bae, Y. K. Han, T. J. Park, Y. S. Huh and W. K. Hong, *Nanoscale*, 2014, **6**, 8068.

24.   X. Pan, Y. Zhao, G. Ren and Z. Fan, *Chem. Commun.*, 2013, **49**, 3943.

25.   G. Ji, Y. Ma, B. Ding and J. Y. Lee, *Chem. Commun.*, 2012, **24**, 3329.

26.   Z. Xu, H. Wang, Z. Li, A. Kohandehghan, J. Ding, J. Chen, K. Cui and D. Mitlin, *J. Phys. Chem. C*, 2014, **118**, 18387.

27.   Y.-J. Bai, C. Gong, N. Lun and Y.-X. Qi, *J. Mater. Chem. A*, 2013, **1**, 89.

28.   S.-L. Chou, J.-Z. Wang, H.-K. Liu and S.-X. Dou, *J. Phys. Chem. C*, 2011, **115**, 16220.

29.   G.-N. Zhu, Y.-G. Wang and Y.-Y. Xia, *Energy Environ. Sci.*, 2012, **5**, 6652.

30.   Z. Jian, L. Zhao, R. Wang, Y.-S. Hu, H. Li, W. Chen and L. Chen, *RSC Adv.* , 2012, **2**, 1751.

31.   Y. M. Jiang, K. X. Wang, X. Y. Wu, H. J. Zhang, B. M. Bartlett and J. S. Chen, *ACS Appl. Mater. Interfaces*, 2014, **6**, 19791.

32.   C. C. Li, Q. H. Li, L. B. Chen and T. H. Wang, *ACS Appl. Mater. Interfaces*, 2012, **4**, 1233.

33.   A. Nugroho, S. J. Kim, K. Y. Chung, B.-W. Cho, Y.-W. Lee and J. Kim, *Electrochem. Commun.*, 2011, **13**, 650.

34.   K. Mukai, Y. Kato and H. Nakano, *J. Phys. Chem. C*, 2014, **118**, 2992.

35.   Y. Q. Wang, L. Gu, Y. G. Guo, H. Li, X. Q. He, S. Tsukimoto, Y. Ikuhara and L. J. Wan, *J. Am. Chem. Soc.*, 2012, **134**, 7874.

36.   H. Ni, W.-L. Song and L.-Z. Fan, *Electrochem. Commun.*, 2014, **40**, 1.

37. J. M. Feckl, K. Fominykh, M. Doblinger, D. Fattakhova-Rohlfing and T. Bein, *Angew. Chem., Int. Ed.*, 2012, **51**, 7459.

38. Y. Sha, B. Zhao, R. Ran, R. Cai and Z. Shao, *J. Mater. Chem. A*, 2013, **1**, 13233.

39. J. Haetge, P. Hartmann, K. Brezesinski, J. Janek and T. Brezesinski, *Chem. Mater.*, 2011, **23**, 4384.

40. J. Ma, C. Wang and S. Wroblewski, *J. Power Sources*, 2007, **164**, 849.

41. A. D. C. Permana, A. Nugroho, K. Y. Chung, W. Chang and J. Kim, *Chem. Eng. J.*, 2014, **241**, 216.

42. Y. Wang, H. Xia, L. Lu and J. Lin, *ACS NANO*, 2010, **4**, 1425.

43. L. Gao, R. Liu, H. Hu, G. Li and Y. Yu, *Nanotechnology*, 2014, **25**, 175402.

44. J. Chen, L. Yang, S. Fang, S.-i. Hirano and K. Tachibana, *J. of Power Sources*, 2012, **200**, 59.

45. A. Nugroho, S. J. Kim, W. Chang, K. Y. Chung and J. Kim, *J. Power Sources*, 2013, **244**, 164.

46. J. Huang and Z. Jiang, *Electrochem. Solid-State Lett.*, 2008, **11**, A116.

47. Q. Zhou, L. Liu, H. Guo, R. Xu, J. Tan, Z. Yan, Z. Huang, H. Shu, X. Yang and X. Wang, *Electrochim. Acta*, 2015, **151**, 502.

48. C. Wang, Z.-X. Deng and Y. Li, *Inorg. Chem.*, 2001, **40**, 5210.

49. C. Lin, X. Fan, Y. Xin, F. Cheng, M. O. Lai, H. Zhou and L. Lu, *Nanoscale*, 2014, **6**, 6651.

50. L. Shen, C. Yuan, H. Luo, X. Zhang, K. Xu and Y. Xia, *J. Mater. Chem.*, 2010, **20**, 6998.

51. Z. Xu, Z. Li, C. M. B. Holt, X. Tan, H. Wang, B. S. Amirkhiz, T. Stephenson and D. Mitlin, *J. Phys. Chem. Lett.*, 2012, **3**, 2928.

52. H.-G. Jung, S.-T. Myung, C. S. Yoon, S.-B. Son, K. H. Oh, K. Amine, B. Scrosati and Y.-K. Sun, *Energy Environ. Sci.*, 2011, **4**, 1345.

53. L. Sun, J. Wang, K. Jiang and S. Fan, *J. Power Sources*, 2014, **248**, 265.

54. Y.-S. Lin and J.-G. Duh, *J. Power Sources*, 2011, **196**, 10698.

55. W. Liu, J. Zhang, Q. Wang, X. Xie, Y. Lou, X. Han and B. Xia, *Powder Technol.*, 2013, **247**, 204.

56. Z. He, Z. Wang, F. Wu, H. Guo, X. Li and X. Xiong, *J. Alloys Compd.*, 2012, **540**, 39.

57. Y.-S. Lin, J.-G. Duh, M.-C. Tsai and C.-Y. Lee, *Electrochim. Acta*, 2012, **83**, 47.

58. R. D. Shannon, *Acta Crystallogr. A*, 1976, **32**, 751.

59. Z. Li, Z. Xu, X. Tan, H. Wang, C. M. B. Holt, T. Stephenson, B. C. Olsen and D. Mitlin, *Energy Environ. Sci.*, 2013, **6**, 871.

60. B. Key, D. J. Schroeder, B. J. Ingram and J. T. Vaughey, *Chem. Mater.*, 2012, **24**, 287.